ARTICLE

Breakdown in the directional transport of droplets on the peristome of pitcher plants

Jiaqian Li[1], Huanxi Zheng[1], Zhengbao Yang[1] & Zuankai Wang [1,2]

Over the centuries, scientists and engineers have been fascinated by the directional transport of water on the peristome of pitcher plant. Through experimental investigation and theoretical analysis, here we reveal the more complex picture of droplet transport on this peculiar natural surface. First, we demonstrate that in addition to the presence of the asymmetric arch-shaped microcavity with gradient wedge corners and sharp edges, the structural gradient in the first-tier microgroove of the pitcher's peristome also plays an important role in the regulation of the directional droplet transport. Moreover, the directional liquid transport only occurs in a limited condition. Without the intricate control of the interplay between its multiscale structures and multiscale sources of water, as well as the dynamic conditions of water, the preferential directional droplet transport will collapse. The new transport phenomenon and the mechanisms we reveal will provide important insights for the design of asymmetric morphologies for droplet manipulation.

[1] Department of Mechanical and Biomedical Engineering, City University of Hong Kong, Hong Kong 999077, China. [2] Shenzhen Research Institute of City University of Hong Kong, Shenzhen 518057, China. Correspondence and requests for materials should be addressed to Z.W. (email: zuanwang@cityu.edu.hk)

As the most wonderful plants described by Charles Darwin, the insectivorous plant can capture insects with a high level of sophistication in speed and sensitivity[1]. Over the past decades, scientists and engineers have been fascinated by such type of peculiar phenomenon in nature[2–7]. As a representative insectivorous plant, the pitcher plant *Nepenthes alata* has evolved exquisite slippery and frictionless peristome structures that can be wetted by rain, condensation, or nectar secreted by the extrafloral nectaries lining owing to the diverse environmental conditions[8]. As a result, foraging insects which come into contact with the wetted peristome "aquaplaned" slip into the pitcher in very large numbers. Recently, it was shown that the directional liquid transport on the peristome is mainly ascribed to the asymmetric arch-shaped microcavities[9]. The microcavity morphology possesses gradient wedge-shaped corners that are responsible for enhanced Taylor rise[10,11] to drive liquid spreading in the direction toward the outer side of the peristome, and sharp edges that are responsible for strong pinning[12] in the reverse direction.

Extensive efforts have also been devoted to translating the nature's inspiration and fundamental understanding to engineering hierarchical surfaces for a wide range of applications including fluid transport, microfluidics, printing, water harvesting, and oil–water separation[13–23]. Inspired by the slippery and frictionless rim on the pitcher plant, an innovative type of slippery liquid-infused porous surfaces (SLIPS) with the exceptional functions of liquid repellency, low hysteresis, self-healing, and enhanced optical transparency has been designed and applied for a diversity of applications involving fluid transportation, optical sensing, self-cleaning, anti-icing, anti-fogging, and anti-fouling in the extreme environments[24–30]. As an effort to emulate the nature's capability, we have developed a novel bioinspired topological liquid diode[31] that allows for the fast and long-range directional liquid transport of virtually any liquid without the need for external energy, by taking advantage of the coalescence with a thin precursor film spreading rapidly ahead of the advancing edge while preventing the backflow in the reverse direction.

Despite extensive progress, our fundamental understanding of the droplet mechanism on peristome is far from clear. From the structure perspective, it is well known that the pitcher plant is decorated with multiscale physical structures; however, the role of individual roughness on the liquid transport remains elusive. Moreover, owing to the diverse environmental conditions, water droplets can be formed through different mechanisms such as rain, fog, or dew, and thereby giving rise to distinct size distribution. Thus, it is not clear whether the directional transport is vulnerable to a wide range of dynamic conditions and droplet sizes. Thus, the fundamental understanding of the interplay between the multiscale physical structures and multiscale sources of water in a wide range of working conditions is still lacking.

In this communication, we present the unexplored structural gradient in the first-tier microgroove of the natural pitcher's peristome, which plays important role in the regulation of the directional spreading behavior of large-scale droplets. We also experimentally and theoretically demonstrate the stability of the directional liquid transport behavior of dynamic droplets on the peristome surface by illustrating the linear transition between unidirectional spreading regime and breakdown regime. Furthermore, we validate the unidirectional transport of droplet on the peristome surface is intricately dependent on the interplay between the multiscale morphology and multiscale sources of water in a wide range of working conditions.

Results

Effect of gradient roughness on the directional liquid transport. Figure 1a shows the surface morphology of the natural peristome. Similar to the previous finding[9], the surface consists of a wide range of relatively large microgrooves covered by elegant small microgrooves (Fig. 1b, c), as well as asymmetric arch-shaped microcavities (Fig. 1d). The arch-shaped microcavities have an overall upward slope and the tops of arches point towards the outer margin of the peristome. However, different from previous findings[5,9], we find that both the width w (~398.2 ± 54.7 μm) and the depth d (~88.6 ± 25.2 μm) of the large microgrooves diverge gradually from the inner side (Fig. 1b) to outer side (Fig. 1c) as presented in Fig. 1e, f, g. To quantify the gradient effect of first-tier roughness, we define two unique gradient angles, α and β, to describe the almost linear variations in the width and the depth (Fig. 1e). To distinguish the multiscale structures, we refer to the relatively large microgrooves, small microgrooves, and microcavities as the first-tier, second-tier, and third-tier roughness, respectively.

How does the roughness gradient in the first-tier structure of pitcher's rim regulate the droplet transport? To answer this question, we first compared the droplet dynamics between the natural peristome surface and the peristome replica with all the roughness. As shown in Supplementary Fig. 1, the PDMS peristome replica perfectly replicates the hierarchical microstructures on the natural peristome and exhibits the same behavior of unidirectional liquid transport as that on the natural peristome (Fig. 2a). When a small droplet impinges on the natural peristome surface, it first symmetrically spreads driven by the inertia effect[32–34]. At ~36 ms, the rightmost contact line gets pinned and the droplet starts to asymmetrically propagate in the direction towards the outer side of the natural peristome, displaying a typical signature of unidirectional liquid transportation (Fig. 2a, Supplementary Fig. 2 and Supplementary Movie 1). To quantify such a distinct unidirectional spreading behavior, we define the ratio between two horizontal spreading lengths as the rectification coefficient, expressed as $k = L_{out}/L_{in}$, where L_{out} and L_{in} indicate the spreading distances towards the outer side and inner side of the peristome at the horizontal direction, respectively (Fig. 2a). In Fig. 2a, k is measured to be about 1.95. We next compared the droplet behaviors on the peristome replica and a control surface which possesses the first-tier roughness alone. The control surface was first made of PDMS peristome replica, and then its second and third-tier roughness was completely screened by the PDMS (Supplementary Fig. 3). For the control surface with the first-tier roughness alone, the droplet also exhibits an asymmetrical spreading towards the outer side, although the k is a little smaller than that on the peristome replica with all three-tier roughness (Fig. 2b). In contrast, for the artificial PDMS peristome surface where all the three-tier features were completely screened (Supplementary Fig. 3), the droplet displays an almost symmetric spreading, where $k \approx 1.04$ as shown in Fig. 2b. The role of gradient first-tier microgroove in leading to a directional liquid flow can also be demonstrated by infusing a flow within a half-conical channel with a width gradient α and depth gradient β. As shown in Fig. 2c, the infused flow preferentially propagates toward the divergent side. These observations clearly suggest that the roughness gradient in the first-tier structure promotes the droplet transport. Moreover, without the presence of the first-tier roughness, the curved spiral topography of the peristome will naturally leads to an apparent spreading in the lateral direction as well[35].

To gain further insight on the role of the structural gradient in the first-tier roughness, we calculated the capillary force gradient in the divergent microgroove (Supplementary Note 1). We assume that the intrinsic contact angle on the peristome surface is almost zero, $\theta \approx 0°$; the cross-section of the first-tier roughness is a semi-ellipse with a width of w and a depth of d; and the profile of the solid-liquid-vapor interface maintains the same as the liquid
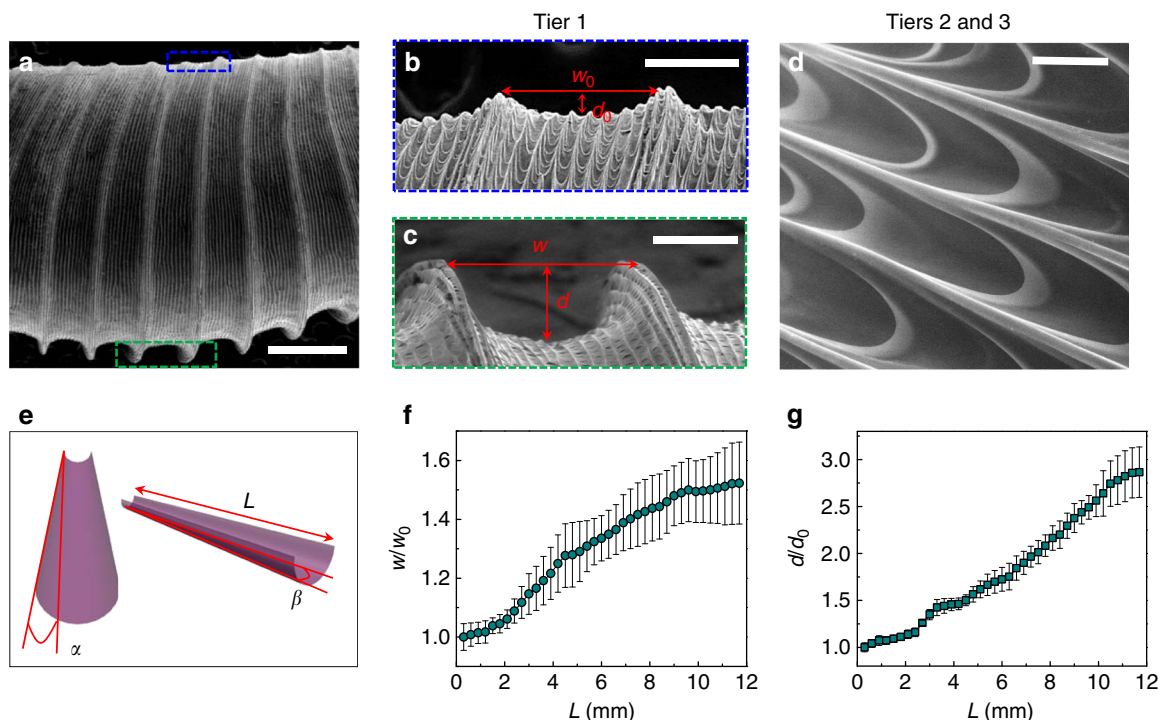
Fig. 1 Topographical characterization of the natural peristome surface. **a** Environmental scanning electron microscope (ESEM) image of the natural peristome from top-view. **b** Magnified ESEM image of the first-tier microgrooves at the inner side of the peristome. **c** Magnified ESEM image of the first-tier microgrooves at the outer side of the peristome. Here w and d are the width and depth of the first-tier microgroove, respectively. **d** Representative ESEM image of the second-tier microgrooves and arch-shaped microcavities. **e** Schematic diagram showing the gradient of the first-tier roughness. α and β are defined as the width gradient and the depth gradient in the first-tier divergent microgroove, and L is the distance to the inner edge. **f** The variation of the normalized width w/w_0 of the first-tier microgroove from the inner side to outer side of the peristome. **g** The variation of the normalized depth d/d_0 of the first-tier microgroove from the inner side to outer side of the peristome. Here w_0 and d_0 are the inlet width and depth at the inner edge of the peristome. These error bars were obtained from the standard deviation of five sets of experimental results. Scale bars: **a** 1 mm, **b** 200 μm, **c** 200 μm, and **d** 30 μm
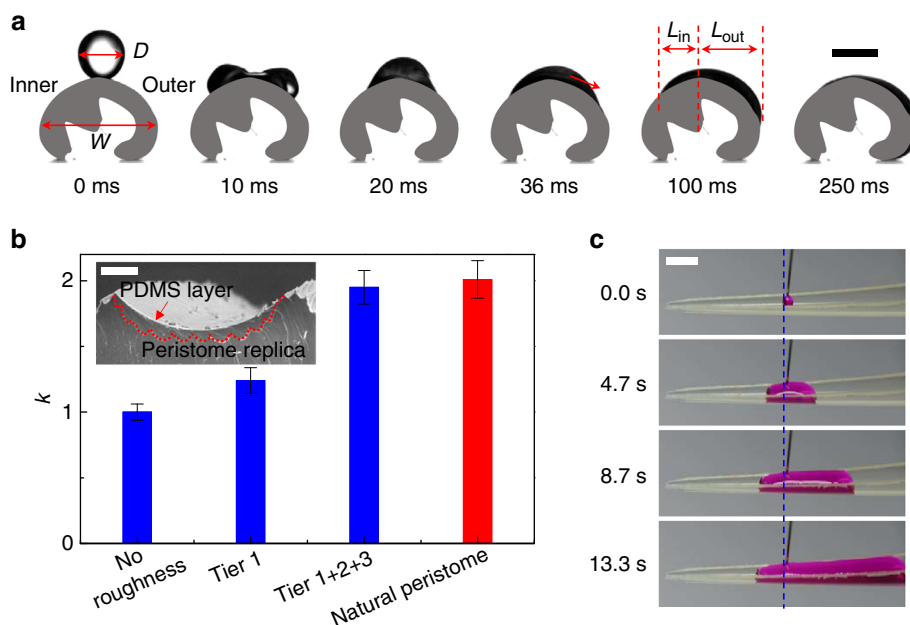

Fig. 2 Capillary gradient in the first-tier roughness on the peristome surface. **a** Selected snapshots of directional liquid spreading when a smaller water droplet impinges a peristome surface. Here D and W indicate the diameter of droplet and the width of peristome, respectively. **b** The variation of k on the natural peristome, peristome replica and control surfaces. The inset SEM image shows the cross-section of the control surface with the first-tier roughness alone. **c** To demonstrate capillary gradient in the first-tier microgroove, we created a half-conical channel with a width gradient α and a depth gradient β. As a water flow is infused in the middle of this channel, the liquid flows preferentially toward the wider side. The error bars for k were obtained from the standard deviation of 5 sets of image data calculation. Scale bars: **a** 2 mm, **b** 100 μm, and **c** 5 mm

front advances (Supplementary Fig. 4). Thus, the capillary force varies as the liquid advances in the divergent channel, and can be quantified as

$$F \approx \gamma L(\lambda \tan\alpha + \lambda \tan\beta - 2\tan\alpha - 2\pi \tan\alpha \tan\beta) + \text{const}$$

$$(1)$$

where γ is the liquid surface tension, λ is the elliptic coefficient and const denotes the constant term of the formula, respectively. Unlike a uniform microgroove with a constant capillary force, an additional driving force gradient (Supplementary Fig. 5) is created along the diverging first-tier roughness towards the outer side as a result of the positive monomial coefficient in the formula of capillary force F. Such a gradient in the capillary force in the first-tier roughness enhances the directional liquid transportation. On the other hand, when the reverse contact line of the droplet gets stably pinned by the defects of sharp edges, the droplet preferentially spreads toward the wider side due to a gradual increase in the interfacial area and the number of arch-shaped cavities in the first-tier roughness. Taken together, we experimentally and analytically reveal the unexplored effect of the structural gradient in the first-tier roughness on the unidirectional droplet spreading behavior on the peristome surface.

Stability of directional liquid transport on the peristome. In addition to elucidating the unexplored role of the first-tier roughness, we also find that the directional droplet transport is only limited to a certain working conditions. In nature, the raindrop[36,37] has a typical diameter ranging from 0.67 to 5 mm and an intrinsic impinging velocity from 2 to 9 m s^{-1}. To imitate the transport dynamics of natural raindrops on the peristome, we first vary the height of falling droplet to obtain diverse impacting velocities. Figure 3 shows the transport dynamics of a impinging droplet on the peristome surface under different impacting velocities or Weber number $We = \rho v^2 D/(2\gamma)$, where ρ is the liquid density, v is the impinging velocity of the falling drop and D is the droplet diameter, respectively. Our experimental results reveal that the manifestation of the unidirectional spreading regime is intricately dependent on the interplay between the Weber number of the droplet and the hierarchical structure of the peristome. Specifically, at smaller We, the droplet displays a unidirectional

spreading behavior, in which the rightmost contact line propagates toward the outer side of peristome while the backflow gets stably pinned (Fig. 2a). With the We increasing, the rectification coefficient k and the spreading time t of the droplet gradually reduce owing to the increased kinetic energy of the droplet (Supplementary Fig. 6). Beyond a critical value of We, the droplet symmetrically reaches the inner and outer edge of the peristome, exhibiting an apparent departure from the asymmetric spreading (Supplementary Fig. 7 and Supplementary Movie 2), referred to as the breakdown regime. The critical We to distinguish the crossover between the unidirectional spreading regime and the breakdown regime also increases with the rise in the peristome width. To theoretically analyze the transition between two distinct spreading regimes, we compared the energy landscape of an impinging droplet with the pinning energy associated with the special hierarchical structures. The initial kinetic energy of the droplet is written as $E_k \approx \rho D^3 v^2 \approx \gamma D^2 We$[38]. The pinning energy on a single sharp edge is $W_0 \approx \gamma ls(\cos\theta_A - \cos\theta_R)$[39,40], where l is the width of third-tier cavity, s is the distance between two neighboring edges, θ_R is the receding angle, and θ_A is the advancing angle as displayed in Fig. 3a. Thus, the total pinning energy of a spreading droplet can be quantified as $W_t \approx \gamma ls(\cos\theta_A - \cos\theta_R)N_{ed}$, where N_{ed} is the number of the sharp edges in the inner half-side of the peristome. We define the kinetic energy of the droplet relative to the pinning energy of hierarchical structures as the breakdown number, which can be expressed as

$$\eta = \frac{E_k}{W_t} \approx \frac{D^2 We}{ls(\cos\theta_A - \cos\theta_R)N_{ed}}$$

$$(2)$$

It is expected that when the kinetic energy E_k is large enough to overcome the pinning effect endowed by the hierarchical structures, the unidirectional spreading behavior of a droplet breaks down.

To simplify the model, the cross-section of the peristome is treated as a circular sector ring with an angle of Φ and a diameter of W, and the droplet reaches both edges of the peristome in the case of breakdown state as shown in Fig. 3a. The advancing contact angle θ_A approximates to zero because of the complete wetting property of the peristome and the receding contact angle θ_R of the droplet ranges between $\theta \leq \theta_R \leq \pi - \varphi + \theta$ as a result
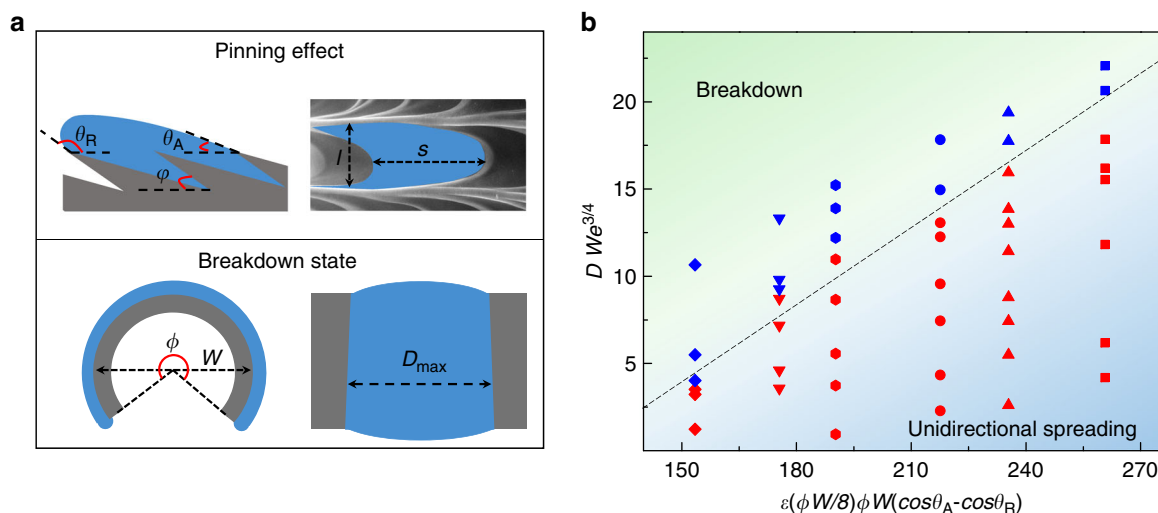

Fig. 3 Spreading behavior transition on the peristome. **a** Schematic diagrams for the pinning effect triggered by sharp edges and the breakdown state. Blue areas and gray areas indicate the liquid and the peristome substrate, respectively. **b** Transition diagram between unidirectional spreading regime and breakdown regime. Red and blue symbols indicate the unidirectional spreading behavior and breakdown behavior, respectively

of the sharp edge effect. Here φ is the angle of the sharp edge, which is ~25° as previously characterized[41]. Moreover, based on the topography of the peristome, the number of sharp edges N_{ed} can be expressed as

$$N_{ed} = \int_0^{\Phi W/4} \frac{\varepsilon(L)w(L)D_{max}}{w(\Phi W/4)ls} \, dL \qquad (3)$$

Here $\varepsilon(L) \approx \frac{w_0 + 2d_0 + \alpha L/2 + \beta L}{4w_0 + 2\alpha L}$ is the roughness of the first-tier microgroove, and $D_{max} \approx DWe^{1/4}$ is the maximum spreading length[42–44] in the lateral direction of the impinging droplet. Thus, the breakdown number can be approximately simplified as

$$\eta \approx \frac{D \, We^{3/4}}{\varepsilon(\Phi W/8)\Phi W(\cos\theta_A - \cos\theta_R)} \qquad (4)$$

As presented in Fig. 3b, the linear transition from the unidirectional spreading regime to the breakdown regime occurs at a critical breakdown number of 0.15. Below the critical η, the impacting droplet stays in the unidirectional spreading regime, whereas at higher η the directional spreading behavior collapses. Note that in our analysis we neglect the viscous energy dissipation during the spreading stage since the inhibition of the backflow is mainly dominated by the pinning effect. Still, there is a good linear correlation between our experimental results and data predicted from the model, suggesting the effectiveness of our simple analytical model to capture the underlying transition physics of the droplet behavior on the peristome surface. This model also builds a link between the structural features, droplet impinging conditions as well as the spreading states. Note that although the structural gradient of the first-tier roughness plays an important role in the regulation of droplet transport in the regime of unidirectional spreading, its effect on the pinning or the suppression of the backflow is negligible compared to the sharp edges.

Droplet size effect on the directional liquid transport. Careful inspection of our analytical model indicates that the breakdown number is proportional to the diameter of the droplet D normalized by the width of the peristome W. Figure 4 displays the transition between the directional spreading regime and

breakdown regime under a function of D/W. When the D/W is smaller than ~0.6, the droplet displays the explicit signature of unidirectional transport behavior on the natural pitcher's rim. In this unidirectional spreading regime, both the rectification coefficient (Fig. 4a) and the spreading time (Fig. 4b) decrease with the increase in the D/W. However, when the D/W is larger than ~0.6, such unidirectional liquid spreading behavior breaks down with the rectification coefficient approximately identical to unity (Fig. 4a) and the spreading time remaining ~10 ms (Fig. 4b). Based on the theoretical model, the breakdown number at this critical D/W is about 0.134, which is consistent with the result shown in Fig. 3b.

Discussion
As discussed earlier, water droplets on the peristome come from multiple sources such as rain, fog, or dew, and thus droplets are vulnerable to a wide range of size distribution. As shown in Fig. 5, condensate droplet[45], which is nucleated from a gas phase with a typical size of <0.3 μm, sticks and accumulates inside the third-tier roughness without contacting the second and first-tier roughness (Supplementary Fig. 8). In this condition, the droplet is also associated with relatively large contact line pinning, without the manifestation of explicit directional motion as in the case of large-scale droplet. When the droplet is large enough to span the second roughness (Fig. 5), as exemplified by fog droplet with diameter of 0.2–100 μm[46,47], it will preferentially spread along the second-tier microgroove towards the direction of the outer side of the peristome. This directional transport is ascribed to the first-tier roughness, which allows for the Taylor rise toward the outer margin of the peristome and strong pinning in the reverse direction. When the droplet such as raindrop[36,37] ranging from 0.67 to 5 mm in diameter is large enough to cover one or more first-tier roughness on the peristome surface (Fig. 5), the first-tier roughness starts to affect the directional flow. In this range, the coupling of capillary force gradient resulting from the first-tier roughness and capillary rise in the third-tier roughness seamlessly activates the directional liquid transport.

In summary, we reveal that the manifestation of the unidirectional transport of droplet is intricately dependent on the interplay between the multiscale physical structures and
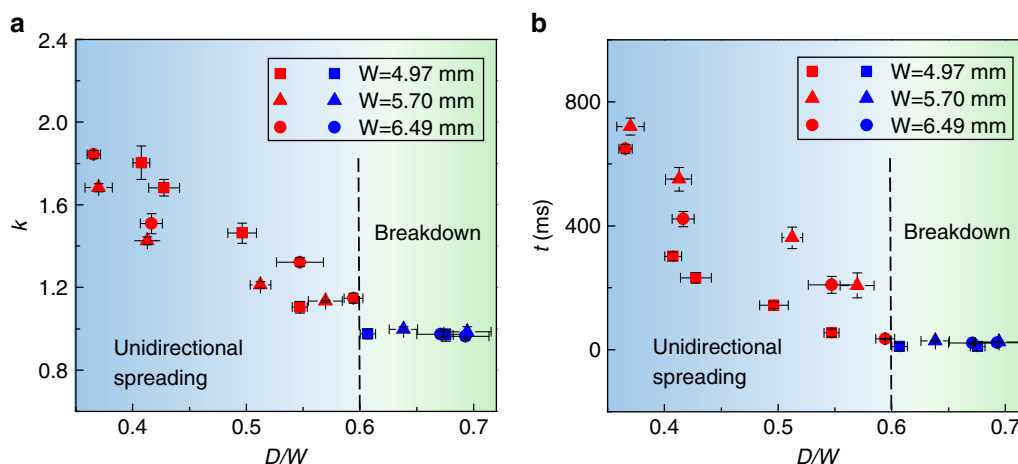

Fig. 4 Effect of the droplet size normalized by the peristome's width on the directional liquid transport. **a** The variation of rectification coefficient k as a function of D/W. **b** The variation of the spreading time t as a function of D/W. When the D/W is below 0.6, the droplet exhibits a unidirectional spreading behavior, while such unidirectional behavior collapses when the D/W is beyond 0.6. At the critical $D/W \approx 0.6$, the breakdown number is calculated to be about 0.134, which is consistent with the theoretical model. Red, blue, and black symbols indicate three different peristomes with widths 4.97 mm, 5.70 mm, and 6.49 mm, respectively. The error bars for t and k were obtained from the standard deviation of 5 sets of experimental results
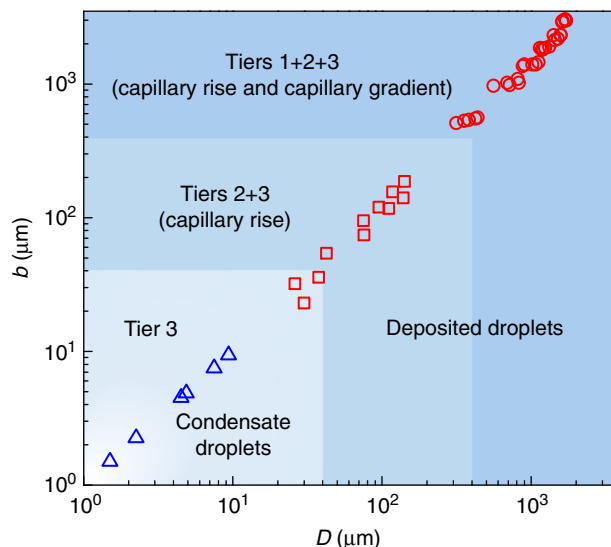
Fig. 5 The interplay between multiscale structures and multiscale sources of droplet on the directional liquid transport. The tiny condensate droplets are randomly nucleated inside the third-tier roughness. Owing to their very small size, there is no directional transport. The fog droplets (red rectangular symbols) spanning one or more second-tier roughness unidirectionally spread toward the outside of the peristome via capillary rise along the wedge-shaped corner and strong pinning in the reverse direction. For the largest raindrop spanning all the roughness, the couple of the capillary rise and capillary gradient enables a unidirectional liquid transport behavior. Here b is the flow width on the peristome surface

multiscale sources of water in a wide range of working conditions. In particular, in contrast to the previous study, we demonstrate that the structural gradient in the first-tier microgroove also plays important role in the regulation of the directional liquid spreading behavior of large-scale droplets. We also experimentally and theoretically examine the stability of the directional liquid transport behavior of large size droplets on the peristome surface by illustrating the linear transition between unidirectional spreading regime and breakdown regime. This work advances our fundamental understanding in the origin and stability of unidirectional liquid transport system on the peristome of pitcher plant, and would provide important insights into the development of novel hierarchical and directional surfaces for a fast long-range liquid self-transportation.

Methods

Fabrication of artificial peristome replicas. We utilized a simple two-step replica molding–casting method to fabricate the artificial peristome replicas of poly-dimethylsiloxane (PDMS). We fabricated three complete peristome replicas from natural peristomes. Afterward, some relatively regular segments of the peristome replicas were chose to manufacture the control surfaces. To investigate the effect of the first-tier roughness on the unidirectional droplet spreading behavior, we coated a layer of uncured PDMS liquid on the artificial replicas by a spin coater (Sawatec Spin Module SM-180 easy) with a high rotational speed of 5000 rpm. The coated artificial peristome replicas were heated immediately at 90 °C for ~1 h to immobilize the PDMS layer. This layer of PDMS screened the second-tier microgrooves and third-tier arch-shaped microcavities. Besides, the process to fabricate the surface without the roughness was basically the same to that developed for the fabrication of the above control surface with the first-tier roughness alone, except that the speed of spin-coating is much smaller, i.e., 500 rpm. To obtain a hydrophilic property, we treated the artificial peristome as well as the control surfaces with a Plasma Cleaner (Harrick Plasma limited.) at high radio frequency level for ~3 min.

Surface characterization. All the natural or artificial samples were characterized by an Environmental Scanning Electron Microscope (ESEM, Quanta™ 250 FEG). The ESEM images of natural peristome and PDMS replica were carefully inspected to verify whether the replication was faithfully conducted. Also, we used the surface

texture tester (Talyor Hobson/Forn Talysurf PGI) to capture the topographical profiles of the artificial PDMS replica and control surfaces. The variation of the first-tier roughness from the inner margin to the outer margin of the peristome was obtained by analyzing the SEM images and topographical profiles. We first cut the PDMS peristome replica into slides and then characterized the cross-section of the slides by using ESEM. The gradient variation in the width and depth of the first-tier microgrooves was calculated based on five different first-tier microgrooves.

Impact experiments. We performed droplet impact experiments on the natural peristome and artificial peristome replicas at room temperature. The distilled water droplet was generated by a syringe at the specific height and impacted on the center of the curved peristome. Impact dynamics was recorded by a high speed camera (Fastcam SA4, Photron limited) from the side view. To investigate the transition between the unidirectional spreading behavior and breakdown behavior, the Weber numbers were varied by controlling and adjusting the heights of the falling droplet. Furthermore, the droplet size was also varied by using stainless steel needles of different sizes.

Condensation on the peristome surface. The natural peristome was put on a cooling plate inside the ESEM. By controlling the temperature of the plate and the vapor pressure inside the chamber, we recorded the formation of the condensate droplet, as well as the droplet behavior inside the third-tier roughness. In this experiment, the temperature of the cooling stage was fixed at ~1 °C. The vapor pressure was gradually increased to ~5.0 Torr, at which the vapor started to nucleate on the surface, and then maintained at ~5.0 Torr during imaging.

Data availability. The data sets generated during and/or analyzed during the current study are available from the corresponding author on reasonable request.

References

1. Ellison, A. M. & Gotelli, N. J. Energetics and the evolution of carnivorous plants—Darwin's 'most wonderful plants in the world'. *J. Exp. Bot.* **60**, 19–42 (2009).
2. Williams, S. E. & Pickard, B. G. Properties of action potentials in drosera tentacles. *Planta* **103**, 222–240 (1972).
3. Hodick, D. & Sievers, A. On the mechanism of trap closure of venus flytrap (dionaea muscipula ellis). *Planta* **179**, 32–42 (1989).
4. Gaume, L., Gorb, S. & Rowe, N. Function of epidermal surfaces in the trapping efficiency of nepenthes alata pitchers. *New Phytol.* **156**, 479–489 (2002).
5. Bauer, U. & Federle, W. The insect-trapping rim of nepenthes pitchers: surface structure and function. *Plant Signal. Behav.* **4**, 1019–1023 (2009).
6. Hsu, C.-P., Lin, Y.-M. & Chen, P.-Y. Hierarchical structure and multifunctional surface properties of carnivorous pitcher plants nepenthes. *JOM* **67**, 744–753 (2015).
7. Zhang, P., Chen, H. & Zhang, D. Investigation of the anisotropic morphology-induced effects of the slippery zone in pitchers of nepenthes alata. *J. Bionic Eng.* **12**, 79–87 (2015).
8. Bohn, H. F. & Federle, W. Insect aquaplaning: nepenthes pitcher plants capture prey with the peristome, a fully wettable water-lubricated anisotropic surface. *Proc. Natl Acad. Sci. USA* **101**, 14138–14143 (2004).
9. Chen, H. et al. Continuous directional water transport on the peristome surface of nepenthes alata. *Nature* **532**, 85–89 (2016).
10. Concus, P. & Finn, R. On the behavior of a capillary surface in a wedge. *Proc. Natl Acad. Sci. USA* **63**, 292–299 (1969).
11. Ponomarenko, A., Quéré, D. & Clanet, C. A universal law for capillary rise in corners. *J. Fluid. Mech.* **666**, 146–154 (2011).
12. Oliver, J. F., Huh, C. & Mason, S. G. Resistance to spreading of liquids by sharp edges. *J. Colloid Interface Sci.* **59**, 568–581 (1977).
13. Hancock, M. J., Sekeroglu, K. & Demirel, M. C. Bioinspired directional surfaces for adhesion, wetting and transport. *Adv. Funct. Mater.* **22**, 2223–2234 (2012).
14. Chu, K.-H., Xiao, R. & Wang, E. N. Uni-directional liquid spreading on asymmetric nanostructured surfaces. *Nat. Mater.* **9**, 413–417 (2010).
15. Malvadkar, N. A., Hancock, M. J., Sekeroglu, K., Dressick, W. J. & Demirel, M. C. An engineered anisotropic nanofilm with unidirectional wetting properties. *Nat. Mater.* **9**, 1023–1028 (2010).
16. Mertaniemi, H. et al. Superhydrophobic tracks for low-friction, guided transport of water droplets. *Adv. Mater.* **23**, 2911–2914 (2011).
17. Stone, H. A., Stroock, A. D. & Ajdari, A. Engineering flows in small devices: microfluidics toward a lab-on-a-chip. *Annu. Rev. Fluid. Mech.* **36**, 381–411 (2004).

18. Park, K. C. et al. Condensation on slippery asymmetric bumps. *Nature* **531**, 78–82 (2016).
19. Ralf, S., Martin, B., Thomas, P. & Stephan, H. Droplet based microfluidics. *Rep. Prog. Phys.* **75**, 016601 (2012).
20. Li, J. et al. Oil droplet self-transportation on oleophobic surfaces. *Sci. Adv.* **2**, e1600148 (2016).
21. Wang, J. Z., Zheng, Z. H., Li, H. W., Huck, W. T. S. & Sirringhaus, H. Dewetting of conducting polymer inkjet droplets on patterned surfaces. *Nat. Mater.* **3**, 171–176 (2004).
22. Li, J. et al. Directional transport of high-temperature janus droplets mediated by structural topography. *Nat. Phys.* **12**, 606–612 (2016).
23. Zheng, Y. et al. Directional water collection on wetted spider silk. *Nature* **463**, 640–643 (2010).
24. Wong, T. S. et al. Bioinspired self-repairing slippery surfaces with pressure-stable omniphobicity. *Nature* **477**, 443–447 (2011).
25. Kim, P. et al. Liquid-infused nanostructured surfaces with extreme anti-ice and anti-frost performance. *ACS Nano* **6**, 6569–6577 (2012).
26. Dai, X., Stogin, B. B., Yang, S. & Wong, T.-S. Slippery wenzel state. *ACS Nano* **9**, 9260–9267 (2015).
27. Leslie, D. C. et al. A bioinspired omniphobic surface coating on medical devices prevents thrombosis and biofouling. *Nat. Biotechnol.* **32**, 1134–1140 (2014).
28. Epstein, A. K., Wong, T. S., Belisle, R. A., Boggs, E. M. & Aizenberg, J. Liquid-infused structured surfaces with exceptional anti-biofouling performance. *Proc. Natl Acad. Sci. USA* **109**, 13182–13187 (2012).
29. Irajizad, P., Hasnain, M., Farokhnia, N., Sajadi, S. M. & Ghasemi, H. Magnetic slippery extreme icephobic surfaces. *Nat. Commun.* **7**, 13395 (2016).
30. Amini, S. et al. Preventing mussel adhesion using lubricant-infused materials. *Science* **357**, 668–673 (2017).
31. Li, J. et al. Topological liquid diode. *Sci. Adv.* **3**, eaao3530 (2017).
32. de Ruiter, J., Lagraauw, R., van den Ende, D. & Mugele, F. Wettability-independent bouncing on flat surfaces mediated by thin air films. *Nat. Phys.* **11**, 48–53 (2015).
33. Liu, Y. et al. Pancake bouncing on superhydrophobic surfaces. *Nat. Phys.* **10**, 515–519 (2014).
34. Hao, C. et al. Superhydrophobic-like tunable droplet bouncing on slippery liquid interfaces. *Nat. Commun.* **6**, 7986 (2015).
35. Li, S., Liu, J. & Hou, J. Curvature-driven bubbles or droplets on the spiral surface. *Sci. Rep.* **6**, 37888 (2016).
36. Tokay, A., Petersen, W. A., Gatlin, P. & Wingo, M. Comparison of raindrop size distribution measurements by collocated disdrometers. *J. Atmos. Ocean. Tech.* **30**, 1672–1690 (2013).
37. Villermaux, E. & Bossa, B. Single-drop fragmentation determines size distribution of raindrops. *Nat. Phys.* **5**, 697–702 (2009).
38. Damak, M., Mahmoudi, S. R., Hyder, M. N. & Varanasi, K. K. Enhancing droplet deposition through in-situ precipitation. *Nat. Commun.* **7**, 12560 (2016).
39. Li, C. et al. Uni-directional transportation on peristome-mimetic surfaces for completely wetting liquids. *Angew. Chem. Int. Ed.* **55**, 14988–14992 (2016).
40. Prakash, M., Quéré, D. & Bush, J. W. Surface tension transport of prey by feeding shorebirds: the capillary ratchet. *Science* **320**, 931–934 (2008).
41. Zhang, P. et al. Bioinspired smart peristome surface for temperature-controlled unidirectional water spreading. *ACS Appl. Mater. Interfaces* **9**, 5645–5652 (2017).
42. Clanet, C., Beguin, C., Richard, D. & Quere, D. Maximal deformation of an impacting drop. *J. Fluid. Mech.* **517**, 199–208 (2004).
43. Lee, J. B. et al. Universal rescaling of drop impact on smooth and rough surfaces. *J. Fluid. Mech.* **786**, R4 (2015).
44. Chantelot, P. et al. Water ring-bouncing on repellent singularities. *Soft Matter* **14**, 2227–2233 (2018).
45. Beysens, D. The formation of dew. *Atmos. Res.* **39**, 215–237 (1995).
46. Pan, Z. et al. The upside-down water collection system of syntrichia caninervis. *Nat. Plants* **2**, 16076 (2016).
47. Podzimek, J. Droplet concentration and size distribution in haze and fog. *Stud. Geophys. Geod.* **41**, 277–296 (1997).

Acknowledgements

Author contributions

Z.W. supervised the research. J.L., H.Z., and Z.W. designed the experiment. J.L. fabricated the samples. J.L. and Z.W. analyzed the data. Z.W., Z.Y., and J.L. wrote the paper. All the authors commented on the paper.

Additional information

Supplementary information accompanies this paper at https://doi.org/10.1038/s42005-018-0038-z.

Competing interests: The authors declare no competing interests.

Reprints and permission information is available online at http://npg.nature.com/reprintsandpermissions/

Publisher's note: Springer Nature remains neutral with regard to jurisdictional claims in published maps and institutional affiliations.